An Online Prediction of Capacity and Remaining Useful Life of Lithium-Ion Batteries Based on Simultaneous Input and State Estimation Algorithm

Tiancheng Ouyang, Peihang Xu, *Student Member, IEEE*, Jingxian Chen, Jie Lu, and Nan Chen

***Abstract*—For lithium-ion batteries used in the electric vehicles, accurate prediction of capacity and remaining useful life online is extremely important. However, most of the research works focus on the prediction accuracy but neglect the complexity of the test environment, which makes many methods show poor robustness in application. To solve the problem, in this article, we first introduce the simultaneous input and state estimation algorithm into the online prediction of state-of-charge and capacity, and combine the Gauss–Hermite extended particle filter to predict the remaining useful life. By setting different gradients of state noises in experiments, the proposed algorithm demonstrates the best accuracy and robustness in comparison with other algorithms. Through the two-factor authentication in simulations, the maximum error of capacity estimation is 35 mAh. For the prediction of remaining useful life, the minimum relative error of the proposed method is 0.4%. Therefore, the high accuracy and strong robustness of the proposed algorithm are verified.**

***Index Terms*—Capacity estimation, Lithium-ion battery, remaining useful life (RUL), simultaneous input and state estimation, state-of-charge (SOC).**

I. Introduction

With the popularity of new energy vehicles represented by electric vehicles (EVs), countries around the world have made great progress in saving energy and reducing emissions for environmental protection and sustainable development [1]–[3]. The number of components used by EVs is about 1/3 less than that of traditional fuel vehicles, which contributes to the industrial intensification and emissions reduction in the areas of manufacturing [4], [5]. Therefore, the popularization of EVs is extremely essential for environmental protection and ensuring energy security [6], [7].

Manuscript received September 16, 2020; revised November 8, 2020; accepted December 10, 2020. Date of publication December 14, 2020; date of current version March 5, 2021. This work was supported by the National Natural Science Foundation of China Under Grant 2018NSFC51805100. Recommended for publication by Associate Editor W. Cao. *(Corresponding author: Tiancheng Ouyang.)*

Tiancheng Ouyang and Peihang Xu are with the Department of Vehicle Engineering, College of Mechanical Engineering, Guangxi University, Nanning 530004, China (e-mail: ouyangtiancheng@gxu.edu.cn; xpeihang@163.com).

Jingxian Chen and Jie Lu are with the Department of Energy and Power Engineering, College of Mechanical Engineering, Guangxi University, Nanning 530004, China (e-mail: chenjingxiann@163.com; lujie_gxu@163.com).

Nan Chen is with the Department of Vehicle Engineering, School of Mechanical Engineering, Southeast University, Nanjing 211189, China (e-mail: nchen@seu.edu.cn).

Color versions of one or more of the figures in this article are available online at https://doi.org/10.1109/TPEL.2020.3044725.

Digital Object Identifier 10.1109/TPEL.2020.3044725

A. Literature Review

As one of the most important component of EVs, the pack is often composed of thousands of cells, and their states need real-time monitoring and accurate evaluation to ensure driving safety and power performance [8].

State-of-charge (SOC) represents the ratio of the available capacity to the overall capacity at the moment, which is the judgment standard for energy strategies in battery management systems (BMS) [9], [10]. For SOC estimation, a large number of literatures have contributed to it. In the battery modeling, the pseudo-two-dimensional model is first proposed by Doyle *et al.* [11], which lays the foundation of electrochemical models. As the first principle model, it can achieve accurate simulation of the internal microreaction of the battery [12]–[15]. The equivalent circuit model (ECM) utilizes a series of circuit elements to simulate the external characteristics and derive the state equations of the battery, which owns good cross-platform adaptability, moderate computational burden, and high model accuracy [16]–[18]. The fractional order model is developed based on the research works of frequency domain characteristics of the battery [19], [20]. The black box model based on artificial neural network can obtain the model parameters by training the dataset, which shows high accuracy compared with the traditional methods [21]–[24]. In parameters identification, the recursive least squares (RLS) [25], [26], genetic algorithm [27], [28] and a series of training algorithms represented by support vector machine are utilized widely [29], [30]. For SOC estimation, there are Ampere-hour integration method [31], look-up table method [32], Kalman filter [33], [34], particle filter (PF) [35], [36], and H infinite filter [37], [38].

State-of-health (SOH) is employed to measure the aging degree of batteries. With the increase of cycles, the available capacity decreases gradually and is often accompanied by the rise of internal resistance [39], [40]. It is generally believed that when the total capacity is less than 80% of the rated capacity, it is not suitable for continued use and the power battery should be replaced duly [41]. For the estimation of battery capacity, the commonly used approaches include degradation model-based method [42], differential voltage analysis (DVA) method [43], incremental capacity analysis (ICA) method [44], and voltage feature extraction method [45]. The degradation model-based method predicts the capacity by historical data obtained in laboratories or early road tests. However, due to the complexity

of actual environment and working conditions, the historical capacity data often deviate from the real capacity degradation trajectory, which accumulates errors in application for online prediction. The principle of DVA/ICA method is to deduce the capacity by studying the influence of aging to the variations of voltage. One method based on voltage feature extraction is to derive the real-time capacity from the ratio of the accumulated charge to the variations of SOC in a sampling interval. This method requires enough accuracy of SOC estimation.

The remaining useful life (RUL) refers to the difference between the historical cycles and the total cycles of the battery. [46]. Accurate prediction of RUL is important to balance the economy and the safety of EVs [47]. The model-based method combines the nonlinear aging model with the improved PF to calculate the RUL and probability density function (PDF) [48]. Data-driven methods are able to obtain the RUL directly through training and screening the experimental dataset based on machine learning theories. However, the data-driven method usually requires a large number of experimental data, which puts forward high requirements for the storage of BMS [49].

The prototype of simultaneous input and state estimation (SISE) algorithm was first proposed by J. D. Glover in 1969 [50]. It was used to solve the problems of state estimation in linear system when the input signal is unknown. For a long time, due to the good performance and strong robustness, this method was widely used for the signal recovery in environmental and geophysical array analysis. In 2004, H. Trinh discussed the application of SISE algorithm in a nonlinear system, introduced Lipschitz nonlinear function, and Ricatti inequality to design an observer in state estimation [51]. With continuous development of SISE algorithm, its merits are gradually emerging.

In the traditional states estimation, the noises from sensors are often underestimated. Sensor noises refer to all signals except the target signal in the sensor circuit. When the output signal is small, the excessive sensor noises often drown out the target signal and make the system identification difficult. Therefore, many algorithms have been developed to solve the problem. In [33], Wang *et al.* proposed a dual extended Kalman filter (EKF) to estimate SOC. However, due to the defects of the algorithm, the state noise is set ideally and too low in experiments, which brings great uncertainties in practice. In [36], an adaptive EKF is combined with PF to estimate SOC. There is no need to set the state noise in PF, thus the method can work well with large state noise. However, the accuracy of PF method is low, and the combination of two algorithms reduces the working efficiency. Therefore, there is an urgent need for an algorithm with high accuracy and resistance to large state noise in states estimation.

B. Contributions of the Work

Considering the nonlinear characteristics of the lithium-ion battery, based on Thevenin model, we not only introduce the SISE algorithm into the online prediction of SOC and capacity for the first time, but also combine the Gauss–Hermite extended particle filter (GH-EPF) algorithm to predict RUL. Five ternary lithium-ion batteries, whose cathode material and anode material are Li(NiCoMn)O_2 and graphite, respectively, are used in this article. For each battery, the rated capacity is 2600 mAh, and the nominal voltage is 3.7 V. Through the two-factor authentication of dynamic stress test (DST) condition and constant current condition, the validity of the proposed method is verified in SOC and capacity estimation. In the RUL prediction, the proposed method achieves the best prediction effect in all four scenarios when the historical cycles are set to 120 cycles, 240 cycles, 400 cycles, and 600 cycles, respectively. The contributions of this article are as follows.

1) SISE algorithm is first introduced into states estimation of the lithium-ion battery to maintain high accuracy and strong robustness against large state noise.
2) By combining the Gauss–Hermite filter with extended PF, the accuracy of predicting RUL is enhanced.
3) In the RUL prediction, the relationship between the historical data and the accuracy of prediction is discussed.

C. Organization of This Article

The remaining sections in this article are as follows. In Section II, the battery models are introduced in detail, including Thevenin model and capacity degradation model. In Section III, the processes of state estimation and capacity prediction are introduced. Section IV introduces the experimental process and the results of simulations. Finally, Section V summarizes the conclusion if this article and the future work.

II. Battery Modeling

In battery modeling, we design Thevenin model and capacity degradation model. The former is used for the joint estimation of SOC and capacity, and the latter is used to predict the RUL. Thevenin model is one of ECM, which owns a set of resistor capacitor network to describe the polarization phenomena in the cell.

A. Thevenin Model for Joint Estimation

The simplified schematic of Thevenin model is displayed in Fig. 1(a). In the frequency domain, the electrical behavior can be expressed as

$$\begin{cases} \dot{U}_p(s) = \frac{I_L(s)}{C_p} - \frac{U_p(s)}{R_p C_p} \\ U_t(s) = OCV(s) - U_p(s) - R_o I_L(s) \end{cases} \tag{1}$$

where I_L represents the current in the circuit and C_p and R_p are the polarization capacitance and resistance, respectively. U_p is the resulting voltage drop on R_p, which is also called polarization voltage. *OCV* indicates the open-circuit voltage, *Ro* represents the ohmic resistance, U_t is the terminal voltage, and the subscript s is the frequency operator.

Through the derivation, the model equation can be expressed as

$$U_{\mathrm{t}}(s) - OCV(s) = -I_L(s)\left(R_o + \frac{R_p}{1 + R_p C_p s}\right). \tag{2}$$

The transfer function $G(s)$ can be written as

$$G(s) = \frac{U_{\mathrm{t}}(s) - OCV(s)}{I_L(s)} = -R_{\mathrm{o}} - \frac{R_p}{1 + R_p C_p s}. \tag{3}$$

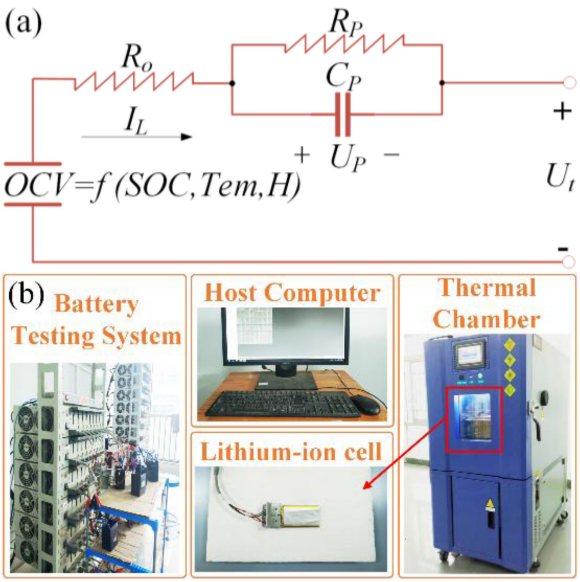

Fig. 1. (a) Simplified schematic of Thevenin model. (b) Test bench.

After a bilinear transformation and discretization, $G(s)$ can be rewritten as

$$s = \frac{2}{T}\frac{1-z^{-1}}{1+z^{-1}} \tag{4}$$

$$G(z^{-1}) = -\frac{\frac{R_oT+R_pT+2R_oR_pC_p}{T+2R_pC_p} + \frac{R_oT+R_pT-2R_0R_pC_p}{T+2R_pC_p}z^{-1}}{1+\frac{T-2R_pC_p}{T+2R_pC_p}z^{-1}} \tag{5}$$

where z denotes the discretization operator. From (5), we can define a_1, a_2, and a_3 as

$$\begin{cases} a_1 = -\frac{T-2R_pC_p}{T+2R_pC_p} \\ a_2 = -\frac{R_oT+R_pT+2R_oR_pC_p}{T+2R_pC_p} \\ a_3 = -\frac{R_oT+R_pT-2R_oR_pC_p}{T+2R_pC_p}. \end{cases} \tag{6}$$

The value of R_O, R_p, C_p, and OCV can all be derived from a_1, a_2, and a_3. Equation (2) can be rewritten as

$$U_t(k) = (1-a_1)OCV(k) + a_1U_t(k-1) + a_2I_L(k) + a_3I_L(k-1). \tag{7}$$

In order to satisfy the calculation form of matrix, we split (7) into the product y_k of two matrices as

$$\varphi_1(k) = [1 \;\; U_t(k-1) \;\; I_L(k) \;\; I_L(k-1)] \tag{8}$$

$$\theta_1(k) = [(1-a_1)OCV(k) \;\; a_1 \;\; a_2 \;\; a_3]^T \tag{9}$$

$$y_k = \varphi_1(k)\theta_1(k). \tag{10}$$

Through verification of plenty of experiments, the OCV is mainly related to SOC, temperature Tem, and cycle history H; and the relationship can be described as

$$OCV = f\left(SOC(t), Tem(t), H(t)\right).$$

It is noticeable that SOC and temperature change sharply during a single discharge. In this article, the cycle history $H(t)$ refers to the number of cycles that the experimental battery has been fully charged and discharged. Therefore, the charge/discharge depth of the battery and current density are controlled to be the same. However, the change of cycle history H is too small in a single discharge, so it is generally believed that $\partial H/\partial t \approx 0$.

When constructing the relationship between OCV, SOC, and temperature, the loading current is constant, thus the terminal voltage can be considered as OCV. The real-time OCV is measured by the battery testing system (BTS) Neware CT-4000. During the characterizations of the cells, the relaxation periods are set to three hours. Finally, all experimental steps follow the specifications in *EV battery test procedures manual*, which is designed by Idaho National Laboratory. In this article, OCV and SOC can be described as

$$\begin{aligned} OCV = f(SOC, Tem) = {} & 3.012 - 0.00367 \cdot Tem + 5.5 \cdot SOC \\ & - 0.003764 \cdot Tem \cdot SOC - 24.09 \cdot SOC^2 + 0.028 \cdot Tem \cdot SOC^2 \\ & + 48.87 \cdot SOC^3 - 0.032 \cdot Tem \cdot SOC^3 - 44.56 \cdot SOC^4 \\ & + 0.01488 \cdot Tem \cdot SOC^4 + 15.296 \cdot SOC^5 \end{aligned} \tag{11}$$

$$SOC(k) = SOC(k_0) - \frac{\int_{k_0}^{k} \eta_c I_L(\tau) d\tau}{C_n} \tag{12}$$

where η_c is coulombic efficiency, $I_L(\tau)$is the load current, and C_n represents the total available capacity. The accumulated charge can be calculated as

$$\Delta Ah = \Delta SOC \cdot C_n. \tag{13}$$

Thus, C_n can be deduced as

$$C_{n,\,k_1:k_2} = \frac{\Delta Ah}{\Delta SOC} = \frac{\int_{k_1}^{k_2} I_L(t)\, dt}{SOC(k_1) - SOC(k_2)} \tag{14}$$

where ΔSOC is the variation of SOC and $C_{n,\,k_1:k_2}$ represents the capacity from k_1 to k_2.

Considering that the ageing process of capacity is extremely slow, a little Gaussian noise r_k is added to replace the noises from sensors in simulations. The discrete state space equation can be described as

$$C_{n,\,k+1} = C_k + r_k. \tag{15}$$

When the value of capacity is obtained, the SOH can be calculated by

$$SOH(k) = \frac{C_{n,\,k}}{C_{n,\,rated}}. \tag{16}$$

B. Capacity Degradation Model

For capacity degradation model, due to the good consistency between curve and the experimental data, exponential growth model is widely employed to predict the capacity degradation [42]. Through the experiments, battery capacity fade is closely related to the internal impedance increase, thus this model can well characterize the nonlinear trend of capacity fade and is simple enough for on-board applications. Hence, the model of

capacity degradation can be expressed as

$$C_{n,\,k} = a \cdot \exp(b \cdot k) + c \cdot \exp(d \cdot k) \tag{17}$$

where k represents the number of cycles and $C_{n,k}$ denotes the remaining capacity after k cycles. In addition, a, b, c, and d are uncertain parameters with Gaussian noise, which need to be identified.

The state space equations are as follows:

$$X(k) = [a(k),\ b(k),\ c(k),\ d(k)]^T \tag{18}$$

$$\begin{cases} a(k+1) = a(k) + \omega_a(k), & \omega_a \sim N(0,\ \sigma_a) \\ b(k+1) = b(k) + \omega_b(k), & \omega_b \sim N(0,\ \sigma_b) \\ c(k+1) = c(k) + \omega_c(k), & \omega_c \sim N(0,\ \sigma_c) \\ d(k+1) = d(k) + \omega_d(k), & \omega_d \sim N(0,\ \sigma_d). \end{cases} \tag{19}$$

Therefore, the observation equation is as follows:

$$C(k) = a(k) \cdot \exp(b(k) \cdot k) + c(k) \cdot \exp(d(k) \cdot k) + v(k) \tag{20}$$

where *C(k)* is set to 80% of the rated capacity in general calculation. With the iterations of *X(k)* and the uncertain parameters a, b, c, and d, we can obtain the value of k, which is the number of cycles.

III. State Estimation

A. Parameters Identification

After completing the battery modeling, the model parameters need to be identified. As a commonly used method of data - driven methods, the RLS algorithm can search the best function matching of data and find the unknown solution by minimizing the squares of state errors. However, in dealing with a large number of similar or irregular samples, the capability to correct the identification errors declines obviously, which is called the data saturation phenomenon. Therefore, the variable forgetting factor (VFF) is introduced to reduce errors by losing a part of historical data to strengthen the identification performance. The related formulas are realized as

$$y_k = \varphi_n(k)\theta_n(k) + e(k) \tag{21}$$

$$e(k) = U_t(k) - \varphi_n(k)\hat{\theta}_n(k-1) \tag{22}$$

$$K(k) = \frac{P_n(k-1)\varphi_n^T(k)}{\lambda_n(k-1) + \varphi_n^T(k)P_n(k-1)\varphi_n^T(k)} \tag{23}$$

$$P_n(k) = \frac{P_n(k-1) - K(k)\varphi_n^T(k)P_n(k-1)}{\lambda_n(k-1)} \tag{24}$$

$$\beta_n(k) = 2^{\rho e^2(k)} \tag{25}$$

$$\lambda_n(k) = \lambda_{\min} + (1 - \lambda_{\min})^{\beta_n(k)} \tag{26}$$

$$\hat{\theta}_n(k) = \hat{\theta}_n^-(k) + K(k)e(k) \tag{27}$$

where $\hat{\theta}_n(k)$ is the estimation of vector θ_n, $e(k)$is the estimate error of $U_L(k)$, $K(k)$is the Kalman gain, $P_n(k)$denotes the covariance, λ_n represents VFF, $\lambda_{\min}$ is the constrained minimum value of λ_n, $\beta_n$is the adaptive parameter, and ρ is an empirical index to change the variation rate of λ_n.

TABLE I
PROCESS OF JOINT ESTIMATION BASED ON SISE ALGORITHM

Initialization: For k=0, set: $\hat{x}_0^+ = E_L[x_0]$, $P_0^+ = E_L\left[\left(x_0 - \hat{x}_0^+\right)\left(x_0 - \hat{x}_0^+\right)^T\right]$

Set state equation x_k and observation equation y_k :

$$\begin{cases} x_k = f(x_{k-1}, u_{k-1}) + \omega_{k-1} = A_{k-1}x_{k-1} + B_{k-1}u_{k-1} + \omega_{k-1} \\ y_k = h(x_k, u_k) + \nu_k = C_k x_k + D_k u_k + \nu_k \end{cases}$$

Space equation after discretization:

$$\begin{cases} U_t(k) = OCV(k) - I_L(k)R_o - U_p(k) \\ U_p(k) = U_p(k-1)e^{-\Delta t/\tau_p} + I_L(k-1)R_p(1 - e^{-\Delta t/\tau_p}) \end{cases} \tag{28}$$

Set: $x_k = \left[U_p(k), SOC(k)\right]^T$, $y_k = U_t(k)$, $u_k = I_L(k)$

Define: $A_k = \begin{pmatrix} e^{-\Delta t/\tau_p} & 0 \\ 0 & 1 \end{pmatrix}$, $B_k = \begin{pmatrix} R_p(1 - e^{-\Delta t/\tau_p}) \\ \dfrac{\eta_t \Delta t}{C_k} \end{pmatrix}$,

$$C_k = \left.\frac{\partial U_t}{\partial x}\right|_{x=\hat{x}_k^-} = \left[-1,\ \frac{dU_{OC}(k)}{dSOC(k)}\right], D = -R_0$$

(1) SOC estimation

Step 1: For $k = 1, 2, \ldots\ldots$,

Prior state estimation: $\hat{x}_k^- = A_{k-1}x_{k-1} + B_{k-1}u_{k-1} + \omega_{k-1}$ (29)

Step 2: Prior covariance calculation: $P_k^- = A_{k-1}P_{k-1}A_{k-1}^T + Q_{k-1}$ (30)

Step 3: Innovation: $e_k = \left|y_k - C_k A_{k-1}\hat{x}_k^-\right|$ (31)

Step 4: Kalman gain matrix: $K_k = P_k^- C_k^T (C_k P_k^- C_k^T + R_k)^{-1}$ (32)

Step 5: Disturbance gain matrix:

$$M_k = [B_k^T C_k^T (C_k P_k C_k^T + R_k)^{-1} C B_k]^{-1} B_k^T C_k^T (C_k P_k C_k^T + R_k)^{-1} \tag{33}$$

Step 6: Update the error covariance:

$$\begin{aligned} P_k^+ = {} & (I - K_k C_k)[(I - B_k M_k C_k)P_k^-(I - B_k M_k C_k)^T \\ & + B_k M_k R_k M_k^T B_k^T] + K_k R_k M_k^T B_k^T \end{aligned} \tag{34}$$

Step 7: Update the disturbance: $d_k = M_k e_k$ (35)

Step 8: Update the state estimation:

$$\hat{x}_k^+ = A_k \hat{x}_k^- + B_k d_k + K_k(e_k - C_k B_k d_k) \tag{36}$$

(2) Capacity calculation

Step 9: Variation of SOC calculation: $\Delta SOC_k = \hat{x}_k^+(2,:) - \hat{x}_{k-1}^+(2,:)$ (37)

Step 10: Accumulated charge calculation: $\Delta Ah_k = \int_{k-1}^{k} I_L(t)\,dt$ (38)

Step 11: Capacity calculation: $C_{n,\,k} = \dfrac{\Delta Ah}{\Delta SOC}$ (39)

B. State-of-Charge and Capacity Joint Estimation

For the joint estimation of SOC and capacity, considering the difference between their time-varying speeds, the common method is multiscale double Kalman filters. The advantage of this method lies on precise results, less interference by noise and light burden of calculation. However, the disadvantage is that the algorithm environment is too idealized, and it is often difficult to estimate the capacity accurately. In addition, this method does not take into account the impact of the external environment on the available capacity, thus the results can only be used for reference.

In this article, the prediction of capacity is obtained by the variation of accumulated charge and SOC in the interval. Plenty of tests show that when the battery goes through multiple discharges, the gradual decrease of capacity often leads to the

instability of SOC during the discharge, such as shortening the discharge time, reaching the lower cutoff voltage quickly, and large decrease of SOC within a sampling interval. Therefore, when the accumulated charge per sampling time is constant, the capacity can be estimated through the change of SOC.

The process of joint estimation based on the SISE algorithm is shown in Table I.

C. RUL Prediction

Considering the nonlinear and non-Gaussian characteristics of battery, the PF algorithm has become an ideal approach in the RUL prediction. This method uses a set of randomly weighted particles to construct the *posteriori* PDF, to replace the integral operation with the mean operation, and finally to obtain the state estimation. Therefore, the posterior PDF can be calculated by the accumulated product of particles and correlation weights. However, the variance of the importance weight increases in the iterations, so the importance weight is gradually assembled on relatively few particles. As a result, the sampled particle set cannot approach the posteriori PDF. To solve the particle degradation, resampling is proposed, that is, by copying particles with large weights and abandoning particles with small weights. However, this method usually reduces the diversity of particles and causes depletion of particles. Therefore, choosing a reasonable important density function becomes more and more important in dealing with the particle degradation.

To deal with it, the Gaussian–Hermite (GH) filter and EKF are combined to construct the importance density function of PF algorithm. This method can integrate the latest measurement information to approach the real posteriori probability distribution, which increases the number of effective particles. Among them, the GH filter assumes that both the prediction PDF and the posterior PDF are Gaussian distribution, and estimates the state and its covariance recursively based on the Gaussian filtering framework. The GH filter uses the GH integral to approximate Gaussian distribution integral formula in the recursive process as follows:

$$\int f(x)N(x;\ \mu,\ \sigma)\ dx \approx \sum_{j=1}^{m} \omega_j f(x_j) \tag{40}$$

$$x_j = (\sqrt{\sigma})_j q_j + \mu \tag{41}$$

where $f(x)$ represents a vector polynomial, q_j is the zero point of Hermite orthogonal polynomial, that is, Gaussian point in GH integral.ω_j is the corresponding weight, μ and σ are the mean and covariance matrix of Gaussian distribution, respectively, and m represents the number of Gaussian points.

In addition, since PDF is assumed to be Gaussian distribution in the GH filter, EKF is added to construct the density function twice. EKF is an estimation approach based on recursive minimum mean square error realized by first-order Taylor expansion, which is often used for the local linearization of systems. In the sampling stage, EKF method combines the latest observation information, utilizes the approximate PDF to calculate the mean and covariance for each particle and then uses them to guide the next sampling work.

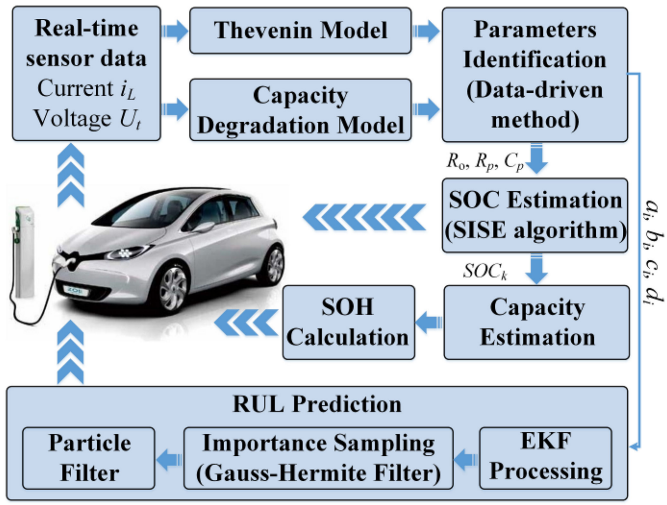

Fig. 2. Overall framework of functions in this article.

The detailed process of the RUL prediction based on GH-EPF method is listed in Table II. The fitting results of parameters for capacity degradation model in five batteries are listed in Table III.

The overall framework of functions in this article is shown in Fig. 2.

IV. Experiments, Simulation, and Analysis

A. Test Bench

The test bench, which consists of a BTS, a host computer, a thermal chamber, and lithium-ion cells, is shown in Fig. 1(b). The host computer is used to operate the testing software and manage the other devices. The thermal chamber can monitor and maintain the operation temperature. The BTS charges and discharges the batteries according to the given program and records the testing data.

The flowchart of battery test is shown in Fig. 3(a). The static capacity test, the reference performance test (RPT), the hybrid pulse test, the OCV test, and the loading profiles test are all included. The static capacity test aims to determine the maximum available capacity of the batteries at different aging stages. The capacity is measured at C/3 rate using three cycles. RPTs at C/20, C/3, C/2, 1C, and 2C are used to evaluate the cell capacity loss at different rates. 3 hours rest is allowed between any charge or discharge process. Then, the residual capacity in the cells at the end-of-charge and end-of-discharge is measured subsequently by a CC step at C/20 until 4.2 and 2.8 V were reached again. The OCV test is carried out to achieve the relationship between SOC and OCV at different aging stages. The cells are charged and discharged at C/3, and OCV at corresponding SOC could be obtained after 3 h rest.

The final results are drawn by sorting, transforming, and fitting the testing data. In Fig. 3(b), when the discharge rate is kept at 0.3C, the amplitude of OCV gradually narrows with the decline of the temperature. When the temperature declines, the rate of the chemical reaction inside the battery decreases

TABLE II
DETAILED PROCESS OF RUL PREDICTION BASED ON GH-EPF METHOD

Initialization: For $j = 0,1,2\cdots$;

Set $\mu_0^+ = E_L[\mu_0], \sigma_0^+ = E_L\left[(\mu_0 - \mu_0^+)(\mu_0 - \mu_0^+)^T\right]$,

State and observation equations:

$$\mu_j^i = f(\mu_{j-1}^i, Z_{j-1}) + \omega_{j-1}, \; y_j = h(\mu_j^i, Z_j) + \nu_j$$

Linearization processing:

$$f(\mu_{j-1}^i, Z_{j-1}) \approx f(\hat{\mu}_{j-1}^i, Z_{j-1}) + \left.\frac{\partial f(\mu_{j-1}^i, Z_{j-1})}{\partial \mu_{j-1}^i}\right|_{\mu_{j-1}^i = \hat{\mu}_{j-1}^i} (\mu_{j-1}^i - \hat{\mu}_{j-1}^i)$$

$$h(\mu_j^i, Z_j) \approx h(\hat{\mu}_j^i, Z_j) + \left.\frac{\partial h(\mu_j^i, Z_j)}{\partial \mu_j^i}\right|_{\mu_j^i = \hat{\mu}_j^i} (\mu_j^i - \hat{\mu}_j^i)$$

Matrices setting: $F_{j-1}^i = \left.\frac{\partial f(\mu_{j-1}^i, Z_{j-1})}{\partial \mu_{j-1}^i}\right|_{\mu_{j-1}^i = \hat{\mu}_{j-1}^i}$

$$G_j^i = \left.\frac{\partial h(\mu_j^i, Z_j)}{\partial \mu_j^i}\right|_{\mu_j^i = \hat{\mu}_j^i}, \; H_j^i = [F_j^i, 1, 1]$$

(1) EKF processing

Prior state estimation: $\mu_{j,pre}^i = f(\mu_{j-1}^i, Z_{j-1})$ (42)

Covariance estimation: $\sigma_{j,pre}^i = F_j^i \sigma_{j-1}^i (F_j^i)^T + G_j^i Q_j (G_j^i)^T$ (43)

Kalman gain: $K_j = \sigma_{j,pre}^i (H_j^i)^T [U_j^i R_j (U_j^i)^T + H_j^i \sigma_{j,pre}^i (H_j^i)^T]^{-1}$ (44)

Posterior state update: $\mu_j^i = \mu_{j,pre}^i + K_j[Z_j - h(\mu_{j,pre}^i)]$ (45)

Covariance update: $\sigma_j^i = \sigma_{j,pre}^i - K_j H_j^i \sigma_{j,pre}^i$ (46)

(2) Importance sampling based on Gauss-Hermite filter

For $i = 1,2,\cdots N$, the importance probability density function $x_{r,j}^i \sim Q(x_{r,j}^i | x_{r,0:j-1}^i, y_{r,1:j})$ is drawn to get new samples $x_{r,0:j}^i = \{x_{r,j}^i, x_{r,0:j-1}^i\}$, $Q(x_{r,j}^i | x_{r,0:j-1}^i, y_{r,1:j}) \sim N(\mu_j^i, \sigma_j^i)$

Based on Cholesky decomposition principle, σ_{j-1}^i can be decomposed to $\sigma_{j-1}^i = S^T S$ .The process of importance sampling is as follows.

Samples calculation: $x_{r,m}^i = S^T Q_m + x_{r,j-1}^i \; (m = 1,\cdots,M)$ (47)

Prior importance PDF prediction: $x_{r,j-1}^i = \sum_{m=1}^{M} f(x_{r,m}^i)\eta_m$ (48)

Variance prediction:

$$\sigma_{j-1}^i = \sum_{m=1}^{M} [f(x_{r,m}^i) - x_{r,j-1}^i] \times [f(x_{r,m}^i) - x_{r,j-1}^i]^T \eta_m + R_1 \quad (49)$$

State correction: $x_{r,j}^i = x_{r,j-1}^i + L_j^i (y_{r,j} - z_j^i)$ (50)

Covariance correction $\sigma_j^i = \sigma_{j-1}^i - L_j^i (\sigma_{xz}^i)^T$ (51)

where $z_j^i = \sum_{m=1}^{M} h(x_{r,m}^i)\eta_m$, η_m is the weight coefficient of Gaussian function,

$L_j^i = \sigma_{xz}^i (R_2 + \sigma_{zz}^i)^{-1}, \sigma_{xz}^i = \sum_{m=1}^{M} (x_{r,m}^i - x_{r,j-1}^i)[h(x_{r,m}^i) - z_j^i]^T \eta_m$, and

$\sigma_{zz}^i = \sum_{m=1}^{M} [h(x_{r,m}^i) - z_j^i][h(x_{r,m}^i) - z_j^i]^T \eta_m$.

(3) Particle filter

Mean value calculation: $\mu_j = \frac{1}{N} \sum_{i=1}^{N} x_{r,j}^i$ (52)

Variance calculation: $\sigma_j = \frac{1}{N} \sum_{i=1}^{N} [(x_{r,j}^i - \mu_j^i)(x_{r,j}^i - \mu_j^i)^T + \sigma_j^i]$ (53)

Weight calculation: $\omega_j^{*,i} = \omega_{j-1}^{*,i} \frac{p(y_{r,j}|x_{r,j}^i) p(x_{r,j}^i | x_{r,j-1}^i)}{Q(x_{r,j}^i | x_{r,0:j-1}^i, y_{r,1:j})}$ (54)

Weight normalization: $\omega_j^i = \omega_j^{*,i} \Big/ \sum_{i=1}^{N} \omega_j^{*,i}$ (55)

Resampling: $N_{eff} = 1 \Big/ \sum_{i-1}^{N} (\omega_j^i)^2$ (56)

State estimation: $\hat{x_{r,j}} = \sum_{i=1}^{N} \omega_j^i x_{r,j}^i$ (57)

RUL prediction:

$$C_{n,j+m}^i = a_j^i \cdot \exp(b_j^i \cdot (j+m)) + c_j^i \cdot \exp(d_j^i \cdot (j+m)) \quad (58)$$

Posterior PDF calculation: $p(C_{n,j+m} | C_{1:j}) \approx \sum_{i=1}^{N} \omega_j^i \delta(C_{j+m} - C_{j+m}^i)$ (59)

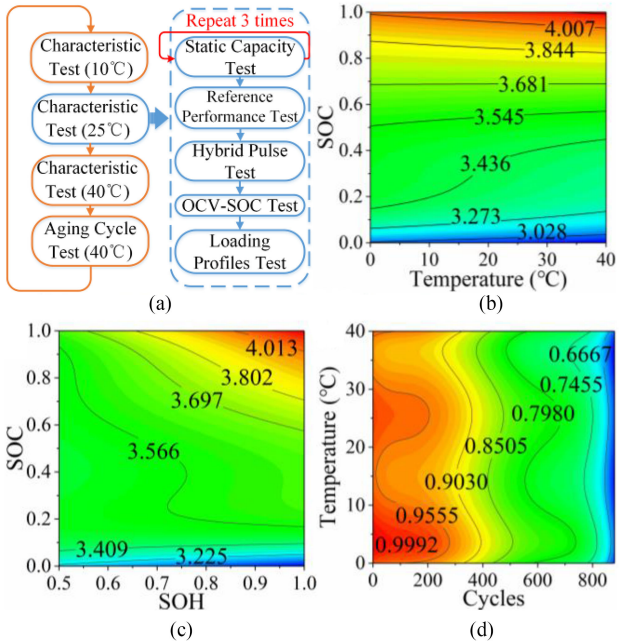

Fig. 3. (a) Flowchart of battery test. (b) Fit map of OCV, temperature, and SOC. (c) Fit map of OCV, SOH, and SOC. (d) Fit map of SOH, cycles, and temperature.

correspondingly and is often accompanied with the shrinkage of available capacity. In Fig. 3(c), with the decrease of battery SOH, the platform of voltage gradually falls. When SOH drops to 0.5, the upper cutoff voltage of the cell drops to 3.62 V, and the voltage level can no longer meet the operating requirements. In Fig. 3(d), we can see that compared with the cycling history, the influence of temperature on SOH is complex but acceptable. In the early stage of the history, when the temperature rises sharply, the chemical reaction rate in the battery increases, but some materials and electrolytes may deteriorate slightly to accelerate the capacity degradation. In contrast, discharge at lower temperature can prolong RUL of the battery.

B. State of Charge Estimation

The hybrid pulse power characteristic (HPPC)current, the corresponding voltage, and the microscopic physical meanings of *OCV*, *Ro,* and R_P are shown in Fig. 4. The microscopic physical meanings of *OCV*, *Ro,* and R_P represent the corresponding phenomena during the charge/discharge, which are related to the time taken into consideration while assessing the voltage drop to calculate the resistance. Generally, OCV can be seen as the terminal voltage when the load current is stable and the polarization phenomenon is slight. Through many experiments, the amplitude of voltage drop is positively correlated with *Ro*. In order to accurately describe the slight voltage drop caused by the polarization phenomenon, R_p is proposed and used in battery modeling. First, we discharge the battery under the HPPC current and obtain the corresponding voltage, which can be used as raw data for parameters identification. Then, the raw data are loaded in the program based on the RLS algorithm. In order to eliminate

TABLE III
FITTING RESULTS OF PARAMETERS FOR CAPACITY DEGRADATION MODEL IN FIVE BATTERIES

Batteries	Lib-01	Lib-02	Lib-03	Lib-04	Lib-05	Mean
a	-0.0001044	-0.0001134	-0.0000975	-0.0001220	-0.0001078	-0.0001090
b	0.009054	0.008826	0.009183	0.008974	0.009265	0.009060
c	2.601	2.626	2.597	2.608	2.632	2.6128
d	-0.0002205	-0.0002279	-0.0002196	-0.0002279	-0.0002361	-0.0002264
R^2	0.9948	0.9876	0.9932	0.9957	0.9864	0.99154
RMSE	0.01445	0.01568	0.01452	0.01398	0.01634	0.01499

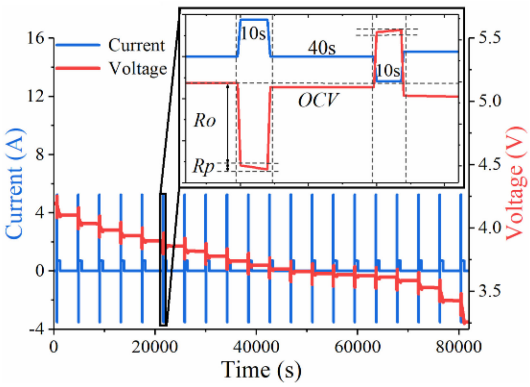

Fig. 4. HPPC current, the corresponding voltage, and the microscopic physical meanings of OCV, R_o, and RP.

TABLE IV
MEDIAN VALUES OF THE PARAMETERS IDENTIFICATION RESULTS

Parameters	Median values
R_O (mΩ)	18.64
R_P (mΩ)	161.8
C_P (kF)	11350

the influences of maximum value and minimum value as much as possible, we select the median values of the identification results instead of the average values. Finally, the median values of the parameters identification results are listed in Table IV.

The results of SOC estimation are shown in Fig. 5. To demonstrate the merits of SISE algorithm against large noise interference, we set up four noise gradients and introduce the unscented Kalman filter (UKF) method and the unscented particle filter (UPF) method for comparison. All simulation experiments were verified by the DST current condition. As shown in Fig. 5(b), when the state noise is set to 1×10^{-10}, the SISE algorithm has the smallest voltage estimation error, but its advantage is not outstanding. From Fig. 5(d), SOC error of the SISE algorithm is larger than that of UKF method in the early stage. This is because the UKF method owns high error correction ability and prediction accuracy when the state noise is set to Gaussian distribution with small value. In the later stage of discharge, SOC error of UKF method gradually exceeds the SISE algorithm. On the one hand, the rise of the polarization internal resistance and the decline of the internal chemical reaction rate make it difficult to accurately estimate SOC. On the other hand, the disturbance control mechanism in SISE algorithm plays an important role, and the principle is as follows.

From (31) to (36), when the absolute error e_k increases suddenly, the change it brought cannot directly affect the Kalman gain matrix K_k and disturbance gain matrix M_k. In other words, the calculation of K_k and M_k is not affected by the sudden increase of error e_k in a cycle, which makes the system ensure the overall stability and robustness at expense of slight accuracy. The update of the error covariance P_k mainly depends on the present values of K_k and M_k, and acts on them in the next round of calculations. Considering the conservatism and lag of K_k and M_k in updating, P_k also becomes conservative and stable in updating, which further improves the robustness in application. Meanwhile, with the rise of e_k, the disturbance d_K rises correspondingly, which makes the final state estimation $\hat{x}_k^+$increase because of the part $B_k d_k$, and it does not satisfy the expected control effect in design. By adding the part $K_k(e_k - C_k B_k d_k)$, this problem can be solved. When e_k increases, d_K increases and causes the part $C_k B_k d_k$ to rise. Because the value of $C_k B_k d_k$ is larger than that of e_k, thus the value of $e_k - C_k B_k d_k$ is negative. In addition, K_k is positive and thus $K_k(e_k - C_k B_k d_k)$is less than 0, which offsets the increase of $B_k d_k$ and finally reduces the update of the state estimation $\hat{x}_k^+$. Generally speaking, when the absolute error e_k rises, the update of the state estimate $\hat{x}_k^+$ decreases accordingly to correct the error. When the absolute error e_k is 0, the update of the state estimate $\hat{x}_k^+$ is 0, which goes to the next round of calculation directly.

From the above principle of SISE algorithm, when the state noise is set ideally, the advantage of the proposed algorithm is not prominent compared with other methods. However, with the increase of state noise, the superiority of SISE algorithm on robustness and prediction accuracy becomes more and more obvious, as shown in Fig. 5(e) to (j). In actual operation conditions, due to the different process standards from a large number of sensors, the state noises are complicated and extremely unstable, which puts forward high requirements for the robustness of algorithms.

The performance of the other two algorithms is different under different state noise. When the state noise is small, the SOC error of UKF method is smaller than that of UPF method. Based on unscented transformation (UT) and KF, UKF method is more sensitive and dependent on Gaussian noise and has a strong ability to correct the estimation error only in a relatively small noise background. UPF method based on UT and PF uses a series of particles to approximate state values, so it has the defects in the estimation accuracy. However, the fact that its non-over-dependent on Gaussian noise makes the UPF algorithm more suitable for uncertain and large noise environments, which explains why the accuracy of UPF method gradually exceeds that of UKF method with the increase of state noise.

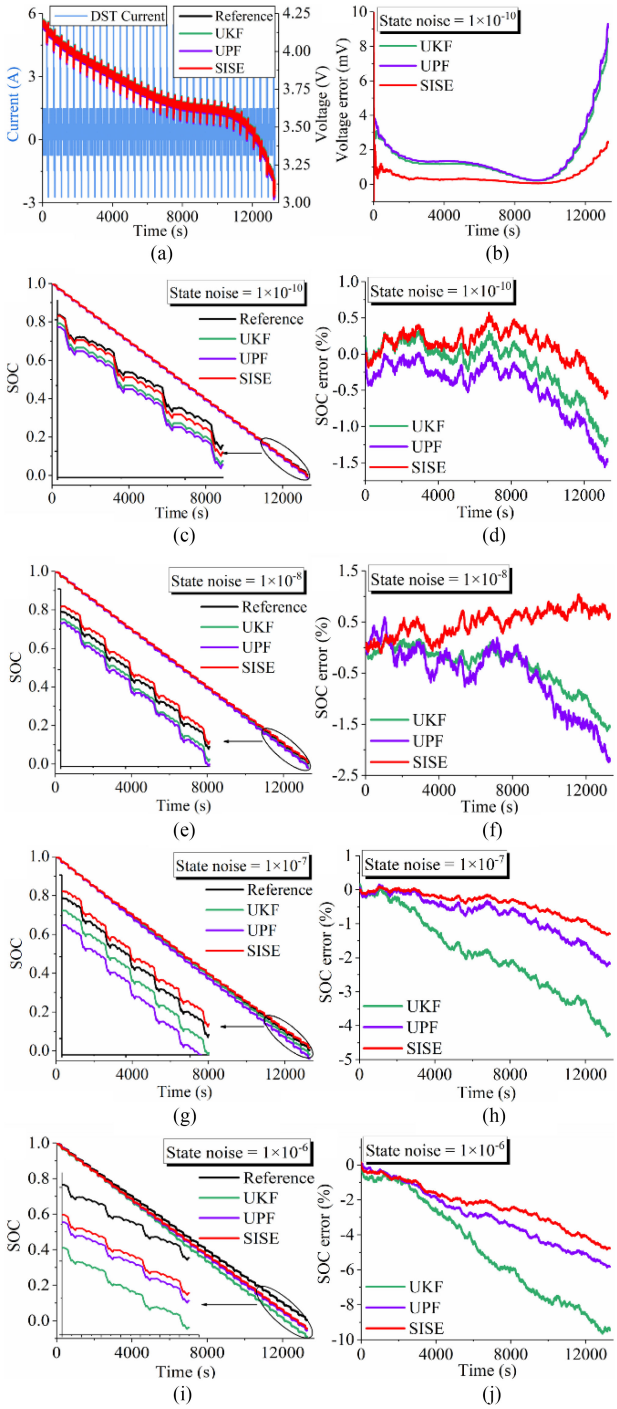

Fig. 5. Results of state of charge estimation. (a) DST current and terminal voltage prediction. (b) Terminal voltage prediction error (state noise = 1×10-10). (c), (e), (g), and (i) are SOC estimation results when state noise is set to 1×10^{-10}, 1×10^{-8}, 1×10^{-7}, and 1×10^{-6}, respectively. (d), (f), (h), and (j) are corresponding SOC estimation error when state noise is set to 1×10^{-10}, 1×10^{-8}, 1×10^{-7}, and 1×10^{-6}, respectively.

C. Capacity Estimation

The definition and connection of capacity, SOH, RUL, and PDF are shown in Fig. 6. Accurate estimation of capacity is the basis of calculating SOH and RUL. In addition, the definition of SOH in different environments is not the same, for example,

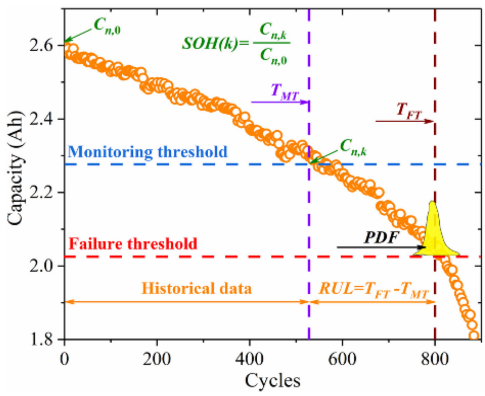

Fig. 6. Definition and connection of capacity, SOH, RUL, and PDF.

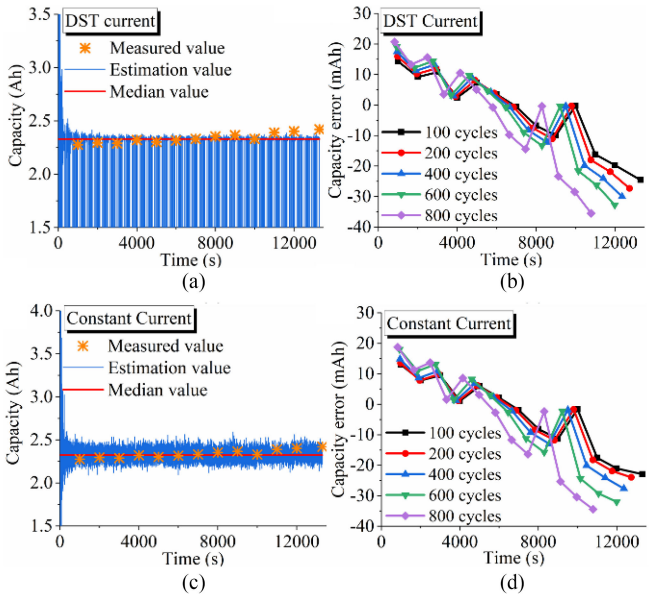

Fig. 7. Results of capacity estimation. (a) Single cycle prediction for the battery with 100 historical cycles under DST current. (b) Capacity error of prediction at different cycle history under DST current. (c) Single cycle prediction for the battery with 100 historical cycles under constant current (0.7 A). (d) Capacity error of prediction at different cycle history under constant current (0.7 A).

internal resistance, capacity, cycle numbers, and deterioration degree of electrode materials can all be used to describe SOH. In this article, SOH is defined as the ratio of $C_{n,k}$ to the rated capacity $C_{n,0}$, so the failure threshold is calibrated at the position where SOH drops to 0.8.

The results of capacity estimation are shown in Fig. 7. In the experiments, we select five batteries with different aging degrees for capacity measurement, and their cycle times were 100, 200, 400, 600, and 800, respectively. For capacity estimation, we take the battery with 100 historical cycles as an example, and carry out simulation under DST current condition and constant current condition (0.7A), respectively, to discuss the relationship between capacity estimation accuracy and battery aging.

It can be seen from Fig. 7(a) and (c), due to the fact that the capacity estimation is related to the real-time current in this

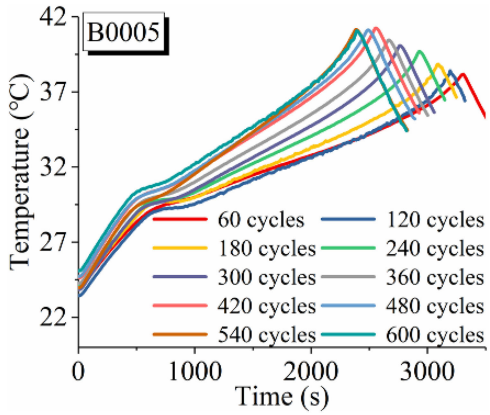

Fig. 8. Temperatures monitoring of the battery with different cycles during the discharge from NASA dataset B0005.

article, the result has some noise. The median values of the estimation results under DST current condition and constant current condition are 2329 and 2324 mAh, respectively, which are consistent with the measured values basically. Theoretically, the capacity of the battery hardly changes during a single discharge, but it can be seen from the measured values that the capacity fluctuates obviously.

To find the reasons, we introduce the experimental battery dataset B0005 from the National Aeronautics and Space Administration (NASA) and the temperatures monitoring of the battery with different cycles during the discharge, as shown in Fig. 8. It can be clearly seen that the change of the temperature is drastic in a single discharge. As the battery ages, the increase of the internal resistance causes the rise of the temperature, which affects the capacity measurement to a certain extent.

From Fig. 7(b) and (d), it can be seen that the accuracy of capacity estimation usually decreases with the increase of aging degree, and there are two reasons: 1) the change of battery temperature brings errors to the capacity measurement; 2) with the increase of aging degree, the available capacity decreases, which makes the battery end discharging to be ahead of schedule under the premise of uniform current conditions, and thus reduces the measured points of capacity. Generally speaking, the error of capacity estimation is acceptable and it is basically not affected by the current conditions.

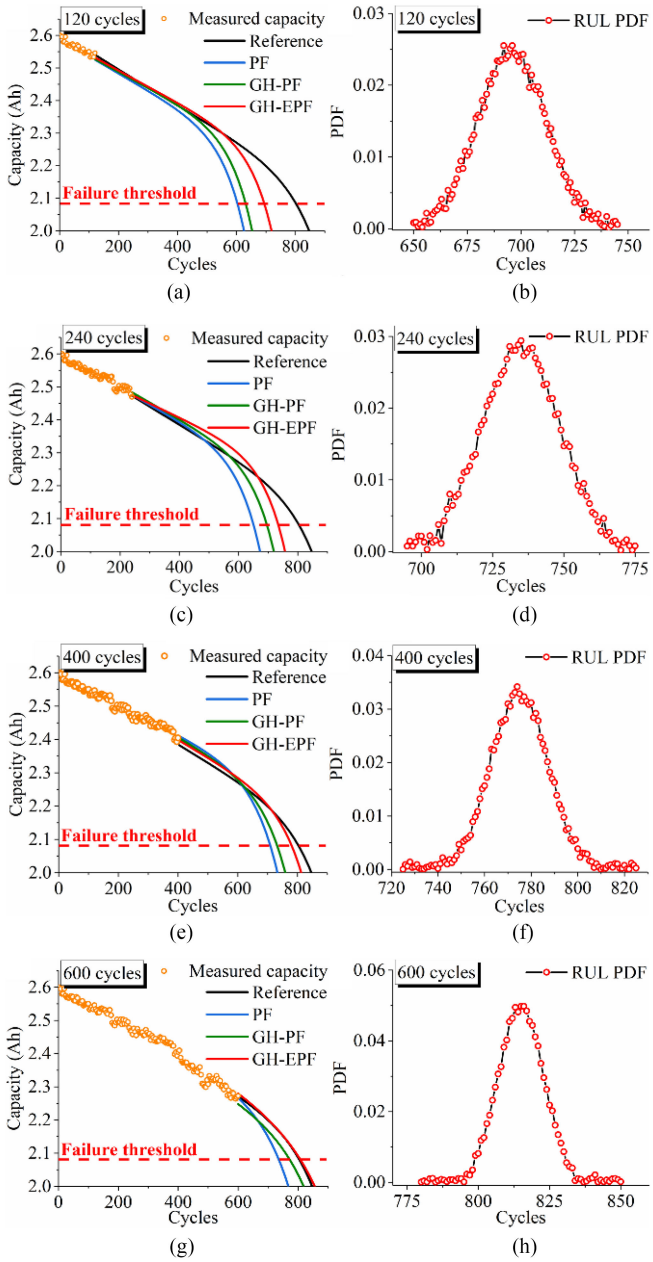

Fig. 9. Results of RUL prediction and PDF calculation. (a), (c), (e), and (g) are RUL prediction at 120, 240, 400, and 600 cycles. (b), (d), (f), and (h) are RUL PDF of the GH-EPF method at 120, 240, 400, and 600 cycles.

D. RUL Prediction

The estimated capacity obtained by above SISE algorithm is used to update the parameters, and GH-EPF method is used to predict the RUL. The results of RUL prediction and PDF calculation are shown in Fig. 9. Among them, the orange hollow circle represents the measured capacity. The black curve is the reference of capacity degradation, which is obtained by fitting the historical data. To fully demonstrate the role of GH-EPF method, we introduce PF method and Gauss–Hermite PF (GH-PF) method for comparison. To explore the relationship between the historical cycles and the prediction accuracy, we set up four monitoring points at 120, 240, 400, and 600 cycles, respectively. When monitoring starting point rises, the historical cycles increase correspondingly.

On the whole, we can see that with the rise of historical cycles, the curves of all methods come close to the reference curve, which means the prediction of RUL rises gradually. In the PDF calculation, when the historical cycles rise, the value of PDF increases, which indicates that the accuracy of RUL calculation increases and the prediction effect is more stable.

From Fig. 9, we can see that PF method first reaches the failure threshold in the later stage, which causes great errors because the importance weight is gradually assembled on relatively few

TABLE V
DETAILED RESULTS OF RUL PREDICTION BASED ON THREE METHODS

Algorithm	PF				GH-PF				GH-EPF			
Monitoring point	120	240	400	600	120	240	400	600	120	240	400	600
Reference cycles	815	815	815	815	815	815	815	815	815	815	815	815
Prediction cycles	604	651	706	732	630	694	735	769	695	736	781	818
Absolute error	211	164	109	83	185	121	80	46	120	79	34	3
Relative error (%)	25.9	20.1	13.4	10.2	22.7	14.8	9.8	5.6	14.7	9.7	4.2	0.4

particles and the sampled particle set cannot approach the real *posteriori* PDF. The GH-PF method constructs the importance density function and integrates the latest information to approach the real posteriori probability distribution. The sampled particles are treated by approximation of Gauss–Hermite integral, then the estimated state and error covariance are taken as the mean and covariance of the Gaussian posterior PDF. It improves the number of effective particles significantly. However, due to the preset Gaussian noise for nonlinear systems, the prediction of GH-PF method still has room for improvement.

On the basis of GH-PF method, GH-EPF introduces EKF processing to reconstruct the importance density function of Gaussian particle filter, which combines the observation information and utilizes the posterior PDF to calculate the mean and covariance for each particle. The detailed results of RUL prediction based on three methods are listed in Table V. It is worth noting that the relative error is defined as the ratio of the absolute error to reference cycles. It can be clearly seen that GH-EPF method owns the best prediction effect while the PF method performs worst. The performance of GH-PF method is between the other two methods.

V. CONCLUSION

In this article, we first introduce the SISE algorithm into online prediction of SOC and capacity, and combine the Gauss–Hermite extended PF to predict the RUL. By comparison with other methods under different state noises, the relatively high accuracy and strong robustness of the proposed method are verified in experiments. The conclusions can be summarized as follows.

1) The SISE algorithm owns relatively high accuracy and strong robustness against the uncertainties and large noises in states estimation. For the SOC estimation, the MAE of the SISE algorithm is less than 0.5% and 5% when state noise in simulation is 1×10^{-10} and 1×10^{-6}, respectively. For capacity prediction, the MAE of the SISE algorithm is less than 1.5% both in DST condition and constant current condition.
2) Due to the construction of Gauss–Hermite filter and EKF to important density function, the accuracy of GH-EPF method on the RUL prediction is enhanced. The relative error of GH-EPF method is 14.7% and 0.4% when the monitoring point is set to 120 cycles and 600 cycles, respectively.
3) Apart from the algorithms, the accuracy of the RUL prediction is also related to the amount of historical data. With the rise of historical data, the monitoring point increases and absolute error of RUL prediction decreases.
4) When building the capacity degradation model, the capacity of five ternary lithium-ion cells with same material is measured under different aging degrees, and the mean value of fitting parameters are selected to minimize errors caused by the differences between batteries. By the experiments, it can be considered that the SISE algorithm is valid for a single cell and a small-scale pack of cells.

In future work, we will carry out in-depth research around the SISE algorithm, including the improvement in stability and accuracy when applied to a large-scale pack of cells under different aging.

REFERENCES

[1] X. Hu, J. Jiang, D. Cao, and B. Egardt, "Battery health prognosis for electric vehicles using sample entropy and sparse Bayesian predictive modeling," *IEEE Trans. Ind. Electron.*, vol. 63, no. 4, pp. 2645–2656, Apr. 2016.
[2] J. Meng, G. Luo, and F. Gao, "Lithium polymer battery state-of-charge estimation based on adaptive unscented Kalman filter and support vector machine," *IEEE Trans. Power Electron.*, vol. 31, no. 3, pp. 2226–2238, Mar. 2016.
[3] H. Rahimi-Eichi, F. Baronti, and M. Y. Chow, "Online adaptive parameter identification and state-of-charge co-estimation for lithium-polymer battery cells," *IEEE Trans. Ind. Electron.*, vol. 61, no. 4, pp. 2053–2061, Apr. 2014.
[4] H. Aung, K. S. Low, and S. T. Goh, "State-of-charge estimation of lithium-ion battery using square root spherical unscented Kalman filter (Sqrt-UKFST) in nanosatellite," *IEEE Trans. Power Electron.*, vol. 30, no. 9, pp. 4774–4783, Sep. 2015.
[5] D. Xiao *et al.*, "Reduced-coupling coestimation of SOC and SOH for lithium-ion batteries based on convex optimization," *IEEE Trans. Power Electron.*, vol. 35, no. 11, pp. 12332–12346, Nov. 2020.
[6] S. Muhammad, M. U. Rafifique, S. Li, Z. Shao, Q. Wang, and N. Guan, "A robust algorithm for state-of-charge estimation with gain optimization," *IEEE Trans. Ind. Inform.*, vol. 13, no. 6, pp. 2983–2994, Dec. 2017.
[7] Y. Feng, C. Xue, Q. Han, F. Han, and J. Du, "Robust estimation for state-of-charge and state-of-health of lithium-ion batteries using integral-type terminal sliding-mode observers," *IEEE Trans. Ind. Electron.*, vol. 67, no. 5, pp. 4013–4023, May 2020.
[8] X. Hu, H. Yuan, C. Zou, Z. Li, and L. Zhang, "Co-estimation of state of charge and state of health for lithium-ion batteries based on fractional-order calculus," *IEEE Trans. Veh. Technol.*, vol. 67, no. 11, pp. 10319–10329, Nov. 2018.
[9] J. Shen, J. Shen, Y. He, and Z. Ma, "Accurate state of charge estimation with model mismatch for li-ion batteries: A joint moving horizon estimation approach," *IEEE Trans. Power Electron.*, vol. 34, no. 5, pp. 4329–4342, May 2019.
[10] D. Wang, F. Yang, K. L. Tsui, Q. Zhou, and S. J. Bae, "Remaining useful life prediction of lithium-ion batteries based on spherical cubature particle filter," *IEEE Trans. Instrum. Meas.*, vol. 65, no. 6, pp. 1282–1291, Jun. 2016.
[11] M. Doyle, T. F. Fuller, and J. Newman, "Modeling of galvanostatic charge and discharge of the lithium/polymer/insertion cell," *J. Electrochem. Soc.*, vol. 140, no. 6, pp. 1526–1533, Jun. 1993.
[12] Z. Song, X. Wu, X. Li, J. Sun, H. F. Hofmann, and J. Hou, "Current profile optimization for combined state of charge and state of health estimation of lithium ion battery based on Cramer–Rao bound analysis," *IEEE Trans. Power Electron.*, vol. 34, no. 7, pp. 7067–7078, Jul. 2019.
[13] S. Dey, B. Ayalew, and P. Pisu, "Nonlinear robust observers for state-of-charge estimation of lithium-ion cells based on a reduced electrochemical model," *IEEE Trans. Control Syst. Technol.*, vol. 23, no. 5, pp. 1935–1942, Jan. 2015.

[14] G. Giordano, V. Klass, M. Behm, G. Lindbergh, and J. Sjoberg, "Model-based lithium-ion battery resistance estimation from electric vehicle operating data," *IEEE Trans. Veh. Technol.*, vol. 67, no. 5, pp. 3720–3728, May 2018.
[15] A. E. Mejdoubi, H. Chaoui, H. Gualous, P. V. D. Bossche, N. Omar, and J. V. Mierlo, "Lithium-ion batteries health prognosis considering aging conditions," *IEEE Trans. Power Electron.*, vol. 34, no. 7, pp. 6834–6844, Jul. 2019.
[16] T. Ouyang, P. Xu, J. Chen, J. Lu, and N. Chen, "Improved parameters identification and state of charge estimation for lithium-ion battery with real-time optimal forgetting factor," *Electrochim. Acta.*, vol. 353, 2020, Art. no. 136576.
[17] N. Wolff, N. Harting, M. Heinrich, F. Roder, and U. Krewer, "Nonlinear frequency response analysis on lithium-ion batteries: A model-based assessment," *Electrochim. Acta*, vol. 260, pp. 614–622, 2018.
[18] X. Lai *et al.*, "A comparative study of global optimization methods for parameter identification of different equivalent circuit models for Li-ion batteries," *Electrochim. Acta*, vol. 295, pp. 1057–1066, 2018.
[19] Y. Wang, G. Gao, X. Li, and Z. Chen, "A fractional-order model-based state estimation approach for lithium-ion battery and ultra-capacitor hybrid power source system considering load trajectory," *J. Power Sources*, vol. 449, 2020, Art. no. 227543.
[20] H. Mu, R. Xiong, H. Zheng, Y. Chang, and Z. Chen, "A novel fractional order model based state-of-charge estimation method for lithium-ion battery," *Appl. Energy*., vol. 207, pp. 384–393, 2017.
[21] Y. Song, D. Liu, H. Liao, and Y. Peng, "A hybrid statistical data-driven method for on-line joint state estimation of lithium-ion batteries," *Appl. Energy*., vol. 261, 2020, Art. no. 114408.
[22] M. Cusenza, S. Bobba, F. Ardente, M. Cellura, and F. Persio, "Energy and environmental assessment of a traction lithium-ion battery pack for plug-in hybrid electric vehicles," *J. Clean. Prod.*, vol. 215, pp. 634–649, 2019.
[23] H. Dai, G. Zhao, M. Lin, J. Wu, and G. Zheng, "A novel estimation method for the state of health of lithium-ion battery using prior knowledge-based neural network and Markov chain," *IEEE Trans. Ind. Electron.*, vol. 66, no. 10, pp. 7706–7716, Oct. 2019.
[24] H. T. Lin, T. J. Liang, and S. M. Chen, "Estimation of battery state of health using probabilistic neural network," *IEEE Trans. Ind. Inform.*, vol. 9, no. 2, pp. 679–685, May 2013.
[25] T. Feng, L. Yang, X. Zhao, H. Zhang, and J. Qiang, "Online identification of lithium-ion battery parameters based on an improved equivalent circuit model and its implementation on battery state-of-power prediction," *J. Power Sources*, vol. 281, pp. 192–203, 2015.
[26] V. Duong, H. Bastawrous, and K. See, "Accurate approach to the temperature effect on state of charge estimation in the LiFePO4 battery under dynamic load operation," *Appl. Energy*, vol. 204, pp. 560–571, 2017.
[27] X. Ding, D. Zhang, J. Cheng, B. Wang, and P. Luk, "An improved Thevenin model of lithium-ion battery with high accuracy for electric vehicles," *Appl. Energy*, vol. 254, 2019, Art. no. 113615.
[28] S. Zhang, J. Qiang, L. Yang, and X. Zhao, "Prior-knowledge independent equalization to improve battery uniformity with energy efficiency and time efficiency for lithium-ion battery," *Energy*, vol. 94, pp. 1–12, 2016.
[29] L. Cai, J. Meng, D.I. Stroe, G. Luo, and R. Teodorescu, "An evolutionary framework for lithium-ion battery state of health estimation," *J. Power Sources*, vol. 412, pp. 615–622, 2019.
[30] C. Sbarufatti, M. Corbetta, M. Giglio, and F. Cadini, "Adaptive prognosis of lithium-ion batteries based on the combination of particle filters and radial basis function neural networks," *J. Power Sources*, vol. 344, pp. 128–140, 2017.
[31] M. Lipu *et al.*, "A review of state of health and remaining useful life estimation methods for lithium-ion battery in electric vehicles: Challenges and recommendations," *J. Clean. Prod.*, vol. 205, pp. 115–133, 2018.
[32] L. Sutter, Y. Firouz, J. Hoog, N. Omar, and J. Mierlo, "Battery aging assessment and parametric study of lithium-ion batteries by means of a fractional differential model," *Electrochim. Acta.*, vol. 305, pp. 24–36, 2019.
[33] L. Wang, D. Lu, Q. Liu, L. Liu, and X. Zhao, "State of charge estimation for LiFePO4 battery via dual extended Kalman filter and charging voltage curve," *Electrochim. Acta*, vol. 296, pp. 1009–1017, 2019.
[34] L. Zheng, J. Zhu, G. Wang, D. Lu, and T. He, "Differential voltage analysis based state of charge estimation methods for lithium-ion batteries using extended Kalman filter and particle filter," *Energy*, vol. 158, pp. 1028–1037, 2018.
[35] X. Tang, K. Liu, X. Wang, B. Liu, F. Gao, and W. Widanage, "Real-time aging trajectory prediction using a base model oriented gradient correction particle filter for Lithium-ion batteries," *J. Power Sources.*, vol. 440, 2019, Art. no. 227118.
[36] Y. Wang, C. Zhang, and Z. Chen, "On-line battery state-of-charge estimation based on an integrated estimator," *Appl. Energy*., vol. 185, pp. 2026–2032, 2017.
[37] D. He *et al.*, "An integrated optimization model of metro energy consumption based on regenerative energy and passenger transfer," *Appl. Energy*., vol. 264, 2020, Art. no. 114770.
[38] F. Zhang, G. Liu, L. Fang, and H. Wang, "Estimation of battery state of charge with H observer: Applied to a robot for inspecting power transmission lines," *IEEE Trans. Ind. Electron.*, vol. 59, no. 2, pp. 1086–1094, Feb. 2012.
[39] Z. Song *et al.*, "The sequential algorithm for combined state of charge and state of health estimation of lithium-ion battery based on active current injection," *Energy*, vol. 193, 2020, Art. no. 116732.
[40] S. Khaleghi, Y. Firouz, J. Mierlo, and P. Bossche, "Developing a real-time data-driven battery health diagnosis method, using time and frequency domain condition indicators," *Appl. Energy*., vol. 255, 2019, Art. no. 113813.
[41] P. Mohtat, S. Lee, J. Siegel, and A. Stefanopoulou, "Towards better estimability of electrode-specific state of health: Decoding the cell expansion," *J. Power Sources*, vol. 427, pp. 101–111, 2019.
[42] W. He, N. Williard, M. Osterman, and M. Pecht, "Prognostics of lithium-ion batteries based on Dempster–Shafer theory and the Bayesian Monte Carlo method," *J. Power Sources*, vol. 196, pp. 10314–10321, 2011.
[43] M. Berecibar, M. Garmendia, I. Gandiaga, J. Crego, and I. Villarreal, "State of health estimation algorithm of LiFePO4 battery packs based on differential voltage curves for battery management system application," *Energy*, vol. 103, pp. 784–796, 2016.
[44] J. Liu, Q. Duan, M. Ma, C. Zhao, J. Sun, and Q. Wang, "Aging mechanisms and thermal stability of aged commercial 18650 lithium-ion battery induced by slight overcharging cycling," *J. Power Sources.*, vol. 445, 2020, Art. no. 227263.
[45] X. Bian, L. Liu, J. Yan, Z. Zou, and R. Zhao, "An open circuit voltage-based model for state-of-health estimation of lithium-ion batteries: Model development and validation," *J. Power Sources.*, vol. 448, 2020, Art. no. 227401.
[46] I. Baghdadi, O. Briat, P. Gyan, and J. Vinassa, "State of health assessment for lithium batteries based on voltage-time relaxation measure," *Electrochim. Acta.*, vol. 194, pp. 461–472, 2016.
[47] Y. Cui *et al.*, "Prediction model and principle of end-of-life threshold for lithium ion batteries based on open circuit voltage drifts," *Electrochim. Acta.*, vol. 255, pp. 83–91, 2017.
[48] F. Cadini, C. Sbarufatti, F. Cancelliere, and M. Giglio, "State-of-life prognosis and diagnosis of lithium-ion batteries by data-driven particle filters," *Appl. Energy*., vol. 235, pp. 661–672, 2019.
[49] G. Ma, Y. Zhang, C. Cheng, B. Zhou, P. Hu, and Y. Yuan, "Remaining useful life prediction of lithium-ion batteries based on false nearest neighbors and a hybrid neural network," *Appl. Energy*., vol. 253, 2019, Art. no. 113626.
[50] J. Glover, "The linear estimation of completely unknown signals," *IEEE Trans. Autom. Control*, vol. 14, no. 6, pp. 766–767, Dec. 1969.
[51] Q. Ha and H. Trinh, "State and input simultaneous estimation for a class of nonlinear systems," *Automatica*, vol. 40, pp. 1779–1785, 2004.

Tiancheng Ouyang received the B.S. and M.S. degrees in power machinery and engineering from Guangxi University, Nanning, China, in 2009 and 2012, respectively, and the Ph.D. degree in vehicle engineering from the Southeast University, Nanjing, China, in 2016.

He did scientific research and completed the Ph.D. dissertation with the Automotive Research Center, Hyundai Kia Automotive Group, Yantai, China, from 2014 to 2016. He was a Postdoctoral Researcher with the Department of Vehicle Engineering, Southeast University, from 2016 to 2018. From 2018 to 2020, he was an Assistant Professor with the Department of Energy and Power engineering, School of Mechanical Engineering, Guangxi University. Since 2020, he has been an Associate Professor with the Department of Vehicle Engineering, School of Mechanical Engineering, Guangxi University. He has published more than 40 peer-reviewed articles. His research interests mainly include electrical/hybrid vehicles, energy recovery and management, battery management system and vibration control of automobile powertrain.

Peihang Xu (Student Member, IEEE) was born in Jingzhou, Hubei Province, China, in 1995. He received the B.Eng. degree in mechanical engineering from the Nanchang Institute of Technology, Nanchang, China, in 2018. He is currently working toward the M.Eng. degree in vehicle engineering with the Department of Mechanical Engineering, Guangxi University, Nanning, China.

His research mainly focuses on battery management system and energy storage system in electric vehicles, including state estimation, reliability, fault diagnosis, and health prognosis.

Jingxian Chen is currently working toward the M.S. degree in power engineering and engineering thermophysics from Guangxi University, Nanning, China.

Her research interests include fuel cell modeling and optimization.

Jie Lu was born in Guangxi, China, in October 1996. He received the B.E. degree in energy and power engineering from Guangxi University of China, Nanning, China, in 2019. He is currently working toward the master's degree in power engineering with the Department of Energy and Power Engineering, Guangxi University, Nanning, China.

His research interests include fuel cell performance testing, optimization, and simulation of energy system.

Nan Chen received the Ph.D. degree in the solid mechanics from the School of Mechanical Engineering, Xian Jiaotong University, Xian, China, in 1988.

From 1992 to 1995, he was a Postdoctoral Researcher with the Institute for Light-duty Structures and Vehicles, Swiss Federal Institute of Technology (ETH), Zurich, Switzerland. Since 1989, he has been with the Department of Vehicle Engineering, School of Mechanical Engineering, Southeast University, Nanjing, China. He is a Professor with the Department of Vehicle Engineering, the Director of Structural Dynamic Optimization Design and Control Research Office, and the Subject Leader Of Doctoral Program in vehicle engineering, Southeast University. His research interests include the vehicle dynamics and control, structural dynamic analysis, and optimization.